

MUON STOPPING POWER AND RANGE TABLES
10 MeV—100 TeV

DONALD E. GROOM

Ernest Orlando Lawrence Berkeley National Laboratory
1 Cyclotron Road, Berkeley, CA 94556, USA
deg@lbl.gov

and

NIKOLAI V. MOKHOV

Fermi National Accelerator Laboratory
Batavia, IL 60510
mokhov@fnal.gov

and

SERGEI I. STRIGANOV

Fermi National Accelerator Laboratory
Batavia, IL 60510
strigano@fnal.gov

and

IHEP, Protvino, Russia

The mean stopping power for high-energy muons in matter can be described by $\langle -dE/dx \rangle = a(E) + b(E)E$, where $a(E)$ is the ionization stopping power and $b(E)$ is the energy-scaled contribution from radiative processes—bremsstrahlung, pair production, and photonuclear interactions. $a(E)$ and $b(E)$ are both slowly-varying functions of the muon energy E . Tables of these stopping power contributions and continuous-slowing-down-approximation (CSDA) ranges (which neglect straggling effects) are given for a variety of elements, compounds, and mixtures for incident kinetic energies in the range 10 MeV to 100 TeV. Tables of the contributions to $b(E)$ are given for the same materials.

1. Introduction

The mean stopping power for high-energy muons (or other heavy charged particles) in a material can be described by [1]

$$\langle -dE/dx \rangle = a(E) + b(E)E, \quad (1.1)$$

where $a(E)$ is the ionization stopping power and $b(E)$ is due to radiative processes—bremsstrahlung, pair production, and photonuclear interactions:

$$b \equiv b_{\text{brems}} + b_{\text{pair}} + b_{\text{nuc}} \quad (1.2)$$

The notation is convenient because $a(E)$ and $b(E)$ are very nearly constant at high energies where radiative contributions are important.

For (approximately) constant a and b , the range of a muon with initial energy E_0 is given by

$$R \approx (1/b) \ln(1 + E_0/E_{\mu c}), \quad (1.3)$$

where $E_{\mu c} = a/b$ is a muon critical energy. The muon critical energy can be defined more precisely as the energy at which ionization and radiative losses are equal, in analogy to one of the ways of defining the critical energy for electrons. It is obtained by finding $E_{\mu c}$ such that

$$a(E_{\mu c}) = E_{\mu c} b(E_{\mu c}). \quad (1.4)$$

The range as obtained from the integral

$$R = \int_0^{E_0} [a(E) + b(E)E]^{-1} dE \quad (1.5)$$

is of limited usefulness, particularly at higher energies, because of the effect of fluctuations. For example, the cosmic ray muon intensity falls very rapidly with energy, so that the flux observed at a given depth underground is dominated by lower-energy muons whose energy-loss fluctuations have allowed them to penetrate more deeply. We nonetheless calculate the “continuous-slowing-down-approximation” (CSDA) range given by Eq. (1.5) as an indicator of actual muon range.

Tables of muon energy loss from a 1985 CERN internal report by Lohmann, Kopp, and Voss [2] have become the *de facto* world standard. This careful work serves as the benchmark for the present effort. Later theoretical work enables us to improve the calculations for low- Z elements ($2 \leq Z \leq 10$) and to make minor improvements elsewhere.

It is our intention to make this report sufficiently self-contained that the interested user can replicate our calculations, even though this results in our giving often-tedious detail. The necessary constants for ionization loss calculations and tables of $b(E)$ for elements, for the mean radiative loss calculations, are available as ascii files at http://pdg.lbl.gov/computer_read.html. These tables are more extensive than the subset of data actually used in this paper.

We present tables of stopping power and mean range for muons from kinetic energy $T = 10$ MeV to 100 TeV for most elements and a variety compounds and mixtures. Tables of $b(E)$ are given for the same materials. In the case of elemental gases, tables are also given for the liquid state.

2. Notation

Table 2.1: Definitions of most of the variables used in this report. The electronic charge e and the kinematic variables $\beta = v/c$ and $\gamma = \sqrt{1 - \beta^2}$ have their usual definitions. β and velocity v are used interchangeably, depending on context. Constants are from *CODATA Recommended Values of the Fundamental Physical Constants: 1998* [3]. In Sect. 5 the convention $c = 1$ is used.

Symbol	Definition	Units or Value
α	Fine structure constant $e^2/4\pi\epsilon_0\hbar c$	1/137.035 999 76(50)
M	Incident particle mass	MeV/ c^2
E	Incident particle energy $\gamma M c^2$	MeV
T	Kinetic energy $(\gamma - 1)M c^2$	MeV
$m_e c^2$	Electron mass $\times c^2$	0.510 998 902(21) MeV/ c^2 MeV
r_e	Classical electron radius $e^2/4\pi\epsilon_0 m_e c^2$	2.817 940 285(31) fm
N_A	Avogadro's number	6.022 141 99(47) $\times 10^{23}$ mol $^{-1}$
ze	Charge of incident particle	
Z	Atomic number of medium	
A	Atomic mass of medium	g mol $^{-1}$
K/A	$4\pi N_A r_e^2 m_e c^2 / A$	0.307 075 MeV g $^{-1}$ cm 2 for $A = 1$ g mol $^{-1}$
I	Mean excitation energy	eV (<i>Note bene!</i>)
δ	Density effect correction to ionization energy loss	
$\hbar\omega_p$	Plasma energy $\sqrt{4\pi N_e r_e^3} m_e c^2 / \alpha$	28.816 $\sqrt{\rho \langle Z/A \rangle}$ eV $^{(a)}$
N_e	Electron density	(units of r_e) $^{-3}$
w_j	Fraction by weight of the j th element in a compound or mixture	
n_j	\propto number of j th kind of atoms in a compound or mixture	
$E_{\mu c}$	Muon critical energy	GeV

$^{(a)}$ For ρ in g cm $^{-3}$.

3. Overview

The behavior of stopping power ($= \langle -dE/dx \rangle$) in copper over twelve decades of muon kinetic energy is shown by the solid curves in Fig. 3.1. Data below the breaks in the curves are from ICRU 49 [4], while data above the breaks are from our present calculations. Approximate boundaries between regions described by different theories or phenomenologies are indicated by the vertical bands. While our main interest is at higher energies, some understanding of the behavior at lower energies is useful, in particular for starting range integrals.

For $\beta \lesssim \alpha Z$, ($T \approx 1$ keV in copper; below the first grey band in Fig. 3.1), the projectile velocity is small compared with that of atomic electrons. Lindhard and collaborators have constructed a successful semi-phenomenological model to describe ionizing energy losses in this regime, approximating the electronic structure of solids by a Fermi distribution [6]. The stopping power is found to be proportional to the projectile velocity. This region is marked by the dashed curve with the dotted extension in Fig. 3.1. However, below $\beta \approx 0.001$ –0.01 nonionizing energy losses via nuclear recoil become increasingly significant [4], finally dominating energy loss at very low energies.

Above $\beta \approx 0.05$ or 0.1 (the second grey band in Fig. 3.1) one may make the opposite approximation, neglecting electronic motion within atoms. There is no satisfactory theory for the

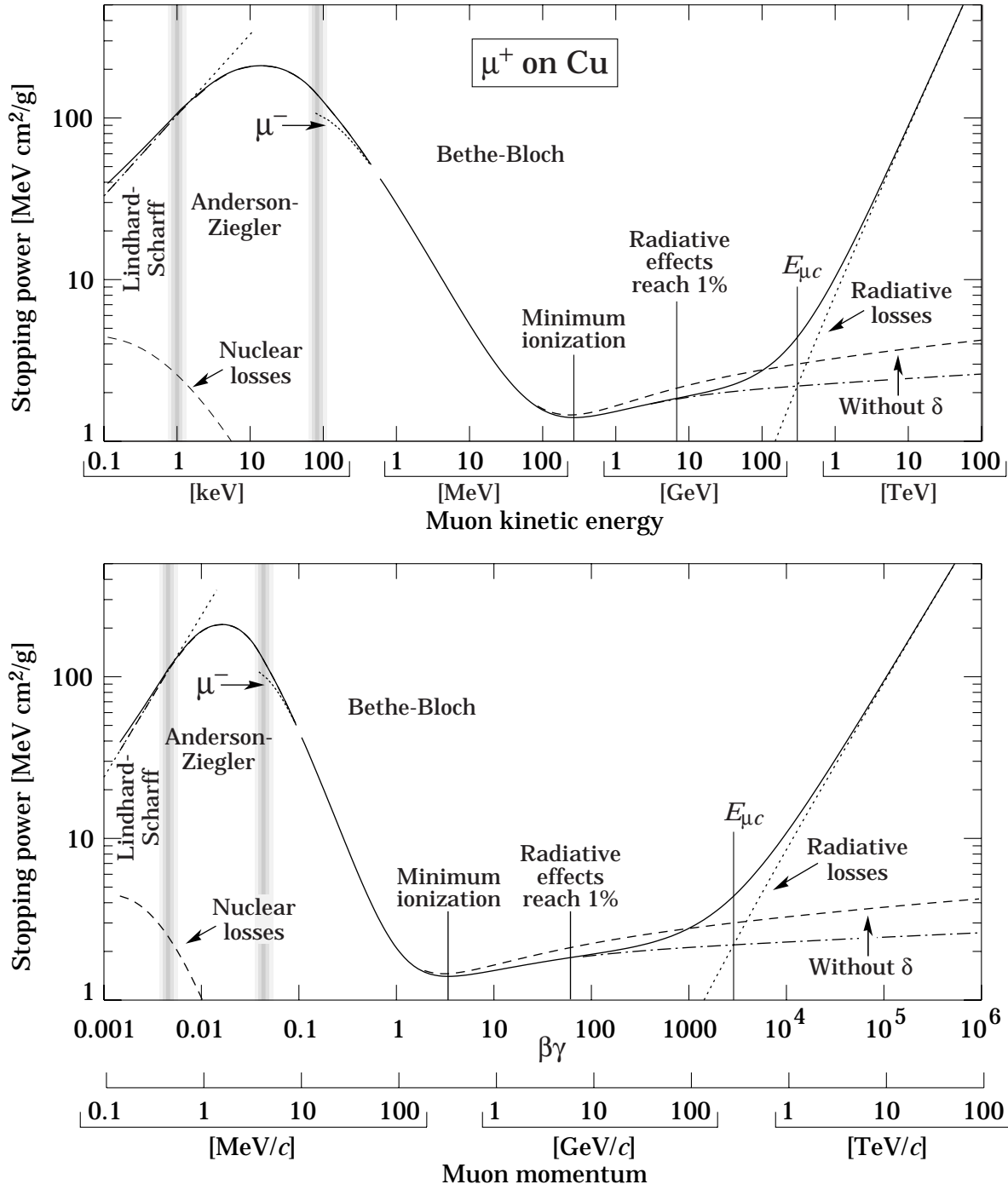


Figure 3.1: Stopping power ($= \langle -dE/dx \rangle$) for positive muons in copper as a function of kinetic energy (top figure, 12 orders of magnitude range) and as a function of $\beta\gamma = p/Mc$ (bottom figure, 9 orders of magnitude). Solid curves indicate the total stopping power. Data below the break at $T \approx 0.5$ MeV are taken from ICRU 49 [4], and data at higher energies are from the present calculations. Vertical bands indicate boundaries between different approximations. The short dotted lines labeled “ μ^- ” illustrate the “Barkas effect” [5]. “Nuclear losses” indicates non-ionizing nuclear recoil energy losses, which dominate at very small energies.

intermediate region, $\alpha Z < \beta < 0.1$ (but see Ref. 7). There is, however, a rich experimental literature, which Anderson and Ziegler have used to construct phenomenological fits bridging the regions in which there is adequate theoretical understanding [8]. This is the interval between the grey bands shown in Fig. 3.1.

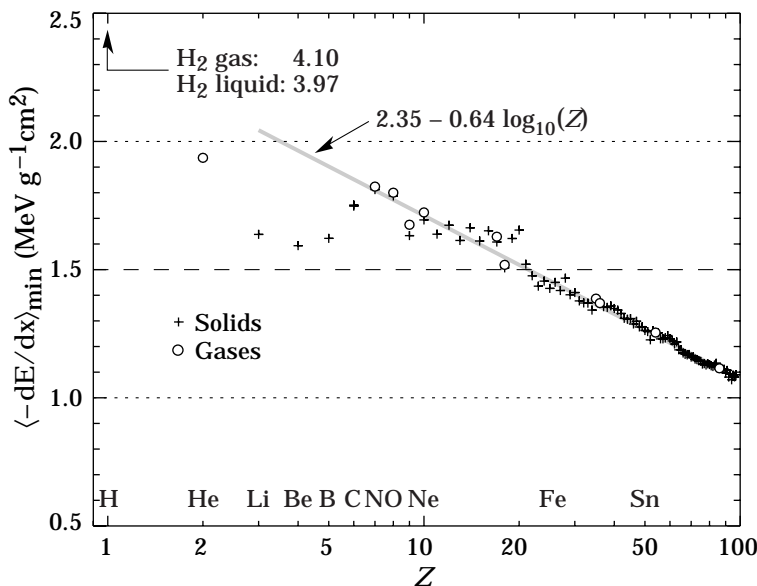


Figure 3.2: Minimum ionization as a function of Z . The straight line is fitted for $Z \geq 6$.

Ionization losses in the high-velocity region are well described by Bethe's theory based on a first-order Born approximation [9], to which are added a number of corrections for the low-energy region and to account for the polarization of the medium at high energies. The curve falls to a broad minimum whose position for solid absorbers decreases from $\beta\gamma = 3.5$ to 3.0 as Z goes from 7 to 100. The mean ionization loss at the minimum value as a function of Z is shown in Fig. 3.2. The rise with further increases of the projectile energy (labeled “without δ ” in Fig. 3.1) is less marked when the polarization effects are taken into account (dash-dotted curve).

Ionization losses at very high energies are somewhat modified by bremsstrahlung from the atomic electrons [10] and other effects, such as form factor corrections [11]. These are of decreased importance because radiative effects rapidly become the dominant energy loss mechanism above a few tens of GeV for even intermediate- Z absorbers. Radiative losses in copper dominate above $E_{\mu c} = 315$ GeV. The radiative contribution, and hence the entire energy loss rate, becomes nearly linear with energy above 1 TeV or so.

4. Ionization energy losses of high-energy heavy particles

The formulae needed to describe the average ionization energy losses of a high-energy ($\beta \gg \alpha Z$) massive (\neq electron) charged particle as it passes through matter have been reviewed elsewhere [4, 12–15]. ICRU 49 is particularly thorough, although it is limited to protons and alpha particles (except for a short π^- table) and to proton energies less than 10 GeV, corresponding to $E < 1.1$ GeV for muons. In this energy region nuclear recoil contributes negligibly to energy loss, and radiative losses can be added as an independent contribution.

For the moment, we leave open the possibilities that the charge is ze and that the particle might be something other than a muon. We briefly review the subject here in order to emphasize high-energy behavior.

4.1. Major contributions

The energy loss rate ($\langle -dE/dx \rangle$, stopping power S , or $a(E)$) is calculated by summing the contributions of all possible scatterings. These are normally from lower to higher energy states, so the particle loses a small amount of energy in each scattering. The kinetic energy of the scattered electron is Q .

The matrix elements needed to find the cross sections are calculated using approximations appropriate to different Q regions. The following summarizes the detailed discussions by Rossi [12] and Fano [13].

1. *Low- Q region.* Here the reciprocal of the 3-momentum transfer (roughly an impact parameter) is large compared with atomic dimensions. The scattered electrons have kinetic energies up to some cutoff Q_1 , and the contribution to the stopping power is

$$S_{\text{low}} = \frac{K}{2} z^2 \frac{Z}{A} \frac{1}{\beta^2} \left[\ln \frac{Q_1}{I^2/2m_e v^2} + \ln \gamma^2 - \beta^2 \right], \quad (4.1)$$

where I is the appropriately weighted average excitation energy. The denominator $I^2/2m_e v^2$ in the first (logarithmic) term is the effective lower cutoff on the integral over dQ/Q . This term comes from “longitudinal excitations” (the ordinary Coulomb potential), and the next two terms from transverse excitations.

The low- Q region is associated with large impact parameters and hence with long distances. Polarization of the medium can seriously reduce this contribution, particularly at high energies where the transverse extension of the incident particle’s electric field becomes substantial. The correction is usually made by subtracting a density-effect term δ , discussed below, inside the square brackets of Eq. (4.1).

2. *Intermediate- and high- Q regions.* In an intermediate region atomic excitation energies are not small compared with Q , but transverse excitations can be neglected. At higher energies Q can be equated to the energy given to the electron, neglecting its binding energy. When the integration of the energy-weighted cross sections is carried out from Q_1 to some upper limit Q_{upper} , one obtains

$$S_{\text{high}} = \frac{K}{2} z^2 \frac{Z}{A} \frac{1}{\beta^2} \left[\ln \frac{Q_{\text{upper}}}{Q_1} - \beta^2 \frac{Q_{\text{upper}}}{Q_{\text{max}}} \right]. \quad (4.2)$$

Here Q_{max} is the kinematic maximum possible electron recoil kinetic energy, given by

$$Q_{\text{max}} = \frac{2m_e c^2 \beta^2 \gamma^2}{1 + 2\gamma m_e/M + (m_e/M)^2}. \quad (4.3)$$

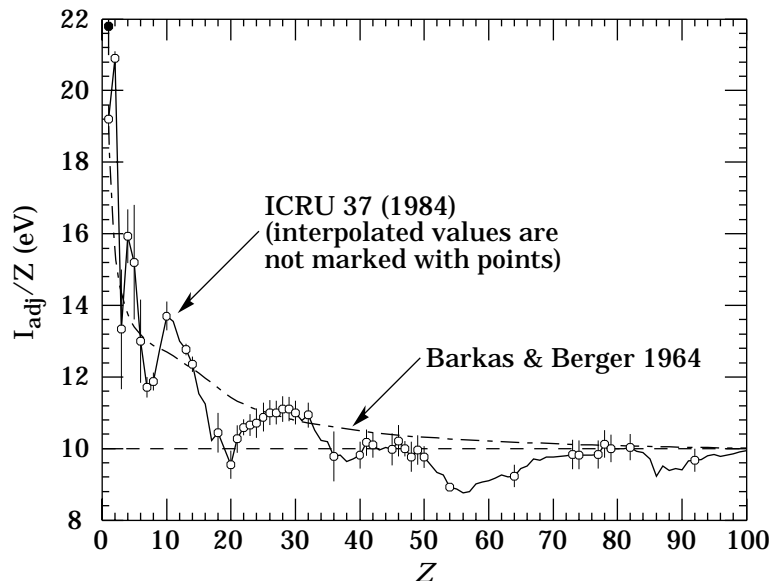


Figure 4.1: Mean excitation energies (divided by Z) as adopted in ICRU 37 [18]. Those based on experimental measurements are shown by symbols with error flags; the interpolated values are simply joined. The solid point is for liquid H_2 ; the open point at 19.2 is for H_2 gas. The dotted curve is from the approximate formula of Barkas [16].

Q_{upper} is normally equal to Q_{max} (as will be the case after the conclusion of this section), and cannot exceed Q_{max} . The more general form given in Eq. (4.2) is useful in considering restricted energy loss, which is of relevance in considering the energy actually deposited in a thin absorber. At high energies the first term in the square brackets dominates. If Q_{upper} is restricted to some maximum value, *e.g.* 0.5 MeV, then S_{high} is essentially constant for $Q_{\text{max}} > Q_{\text{upper}}$. If $Q_{\text{upper}} = Q_{\text{max}}$ the high- Q region stopping power rises with energy as $\ln Q_{\text{max}}$. In other words, the increase of S_{high} with energy is associated with the production of high-energy recoil electrons, or δ -rays.

In Fano's discussion the low-energy approximation $Q_{\text{max}} \approx 2m_e c^2 \beta^2 \gamma^2 = 2m_e p^2 / M^2$ is implicit. Accordingly, Eq. (4.2) is more closely related to Rossi's form (see his Eqns. 2.3.6 and 2.5.4). This low-energy approximation is made in many papers of the Bevatron era, but is in error by a factor of two for a muon with $T = 10.817$ GeV. Note that $Q_{\text{max}} \rightarrow E$ at very high energies.

4.2. Mean excitation energy

"The determination of the mean excitation energy is the principal non-trivial task in the evaluation of the Bethe stopping-power formula" [17]. Recommended values have varied substantially with time. Estimates based on experimental stopping-power measurements for protons, deuterons, and alpha particles and on oscillator-strength distributions and dielectric-response functions were given in ICRU 37 [18]. These were retained in ICRU 49, where a useful comparison with other results is given [4], and they are used in the EGS4 [19] electron/photon transport code. We use them in the present calculations. These values (scaled by $1/Z$) are shown in Fig. 4.1. The error estimates are from Table 2 in Ref. 17. As can be seen, $I/Z \simeq 10 \pm 1$ eV for elements heavier than sulphur. Given the availability of these constants and their sensitivity to atomic shell structure, there is little reason to use the once-common approximate formulae.

4.3. Low-energy corrections

There is no guarantee that a value of Q_1 can be found which simultaneously satisfies the approximation requirements of the high- and low-energy regions. Q_1 is much less than m_e but much larger than (any) electron's binding energy—a situation that becomes paradoxical for high- Z materials and low projectile energies. The standard solution is the addition of an “inner shell correction” term $-2C/Z$ inside the square brackets of Eq. (4.2). A careful modern discussion of this correction is given in Ref. 4. The algorithm is not given completely enough to permit calculation, and depends on unpublished reports which are not generally available.

The shell correction is insignificant at the energies of interest in this report. However, even at intermediate energies it can be significant for “starting” the range integral. To investigate its importance, and to compare our results with the proton dE/dx and range-energy tables in ICRU 49 [4], we have used the now-superseded analytic approximation introduced by Barkas [16]:

$$C = (0.422377\eta^{-2} + 0.0304043\eta^{-4} - 0.00038106\eta^{-6}) \times 10^{-6}I^2 \\ + (3.858019\eta^{-2} - 0.1667989\eta^{-4} + 0.00157955\eta^{-6}) \times 10^{-9}I^3, \quad (4.4)$$

where $\eta = \beta\gamma$ and I is in eV. This form is valid only for $\eta > 0.13$ ($T = 7.9$ MeV for a proton, 0.89 MeV for a muon).

In early Bevatron experiments Barkas *et al.* [5] found that negative pions had a somewhat greater range than positive pions with the same (small) initial energy. This was attributed to a departure from first-order Born theory [20], and is normally included by adding a term $zL_2(\beta)$ to the stopping-power formula. The effect has been measured for a number of negative/positive particle pairs, most recently for antiprotons/protons at the CERN LEAR facility [21]. It is illustrated by the μ^- stopping-power segment shown in Fig. 3.1.

Bethe's stopping power theory is based on a first-order Born approximation. To obtain Bloch's result, a term $z^2L_2(\beta)$ is added if results accurate at low energies are desired.

These corrections are discussed in detail in ICRU 49, and are mentioned here for completeness. They are not significant at the energies of concern in this report.

4.4. Density effect

As the particle energy increases its electric field flattens and extends, so that the distant-collision part of dE/dx (Eq. (4.1)) increases as $\ln \beta\gamma$. However, real media become polarized, limiting this extension and effectively truncating part of this logarithmic rise. This “density effect” has been extensively treated over the years; see Refs. 19, 22, and 23, and references therein. The approach is to subtract a density-effect correction, δ , from the distant-collision contribution, resulting in the $\delta/2$ term in Eq. (4.9). At very high energies,

$$\delta/2 \rightarrow \ln(\hbar\omega_p/I) + \ln \beta\gamma - 1/2, \quad (4.5)$$

where $\hbar\omega_p$ is the plasma energy defined in Table 2.1. A comparison with Eq. (4.9) shows that $a(E)$ grows as $\ln \beta\gamma$ rather than $\ln \beta^2\gamma^2$, and that the excitation energy I is replaced by the plasma energy $\hbar\omega_p$. The effect of the density correction is shown in Fig. 3.1.

At some low energy (related to x_0 below) the density effect is insignificant, and above some high energy (see x_1 below) it is well described by the asymptotic form given in Eq. (4.5). Conductors require special treatment at the low-energy end. Sternheimer has proposed the parameterization [24]

$$\delta = \begin{cases} 2(\ln 10)x - \overline{C} & \text{if } x \geq x_1; \\ 2(\ln 10)x - \overline{C} + a(x_1 - x)^k & \text{if } x_0 \leq x < x_1; \\ 0 & \text{if } x < x_0 \text{ (nonconductors);} \\ \delta_0 10^{2(x-x_0)} & \text{if } x < x_0 \text{ (conductors),} \end{cases} \quad (4.6)$$

where $x = \log_{10}(p/M) = \log_{10} \beta\gamma$. \overline{C} is obtained by equating the high-energy case of Eq. (4.6) with the limit of Eq. (4.5), so that $\overline{C} = 2 \ln(I/\hbar\omega_p) + 1$. The other parameters are adjusted to give a best fit to the results of detailed calculations for $x_0 < x < x_1$. Note that \overline{C} is the negative of the C used in earlier publications. A variety of different parameters are available. In some cases these result from a different fitting procedure having been used with the same model, and although the parameters look different the resulting δ is not sensibly different. For elements, the PEGS4 data [19] use the values from Ref. 26.

In a series of papers by Sternheimer, Seltzer, and Berger, the density-effect parameter tables are extended to nearly 300 elements, compounds, and mixtures.¹ The chemical composition of the materials is given in Ref. 17. The agreement with more detailed calculations or results obtained with other parameter sets is usually at the 0.5% level [25]. We use the tables given in Ref. 22 for most of the present calculations.²

The densities used in these tables are occasionally in error, or, in the case of some polymers with variable density, out of the usual range. The most serious is for the density of SiO₂, for which 2.32 g/cm³ was used in calculating the density-effect parameters. This may be the density of cristobalite. The density of crystalline quartz is about 2.65 g/cm³, and the density of fused quartz is typically 2.20 g/cm³. In this and other cases we use Eq. (Appendix A.8) [23] to adjust the coefficient; such cases are marked by footnotes in Tables 8.1 and 8.2.

There remains the problem of obtaining the density-effect parameters if they have not been tabulated for the material of interest. This issue is of particular importance here in the case of cryogenic liquids such as N₂, but is also of interest when dealing with a compound or mixture not tabulated by Sternheimer, Berger, and Seltzer [22]. The algorithm proposed by Sternheimer and Peierls [23] is discussed in Appendix A.

To some degree, both the adjustment of the parameters for a different density and the Sternheimer–Peierls algorithm can be checked by using those cases in the tables where parameters are given for different densities of the same material. When the “compact carbon” parameters are adjusted to the two other tabulated carbon densities, the difference in stopping power and range with those obtained directly is less than 0.2%. Calculation of parameters for a cryogenic liquid using the Sternheimer–Peierls algorithm can be checked for hydrogen and water. This method was used to calculate parameters for liquid hydrogen at bubble chamber density (0.060 g/cm³), using the excitation energy for the liquid; at worst, at minimum ionization, $\langle -dE/dx \rangle$ was low by 2.5%, while the range was high by 1.1%. Deviations were smaller elsewhere. When the algorithm was used to calculate parameters for water using the excitation energy for steam, the result was 1% higher at minimum ionization than that obtained directly with the water parameters. Only a slight improvement was obtained by using the excitation energy given for water.

Hydrogen is always a worst case, and in any case we scale the parameters from the bubble chamber liquid to those of liquid hydrogen at one atmosphere rather than using the Sternheimer–Peierls algorithm. We conclude that the results in this report obtained with parameters scaled to different densities are accurate to within the 0.5% agreement level estimated by Seltzer and Berger [25], and that the parameters calculated for cryogenic liquids (except hydrogen) using the Sternheimer–Peierls algorithm could be in error by slightly over 1% at minimum ionization, and less elsewhere.

¹ The formula and parameters for lanthanum oxysulfide are corrected in a footnote in Ref. 25.

² Given the power of modern computers, experts now calculate the density effect from first principles rather than use these formulae [27]. One problem along the way is knowing the mean excitation energy, which can be different for condensed and gas states of the same substance and even depends upon density. In our case radiative effects dominate over most of the relevant energy range, and no great error is engendered by using the user-friendly parameterized forms.

4.5. Other high-energy corrections

Bremsstrahlung from atomic electrons in the case of incident muons was considered in a 1997 paper by Kelner, Kokoulin, and Petrukhin [10]. There are four lowest-order diagrams: Photon emission by the muon before and after photon exchange with the electron, and emission by the electron before and after photon exchange. The former diagrams result in losses nearly proportional to E , and are described by Eq. (5.6). The latter are properly part of ionization losses, and produce an additional term in the stopping power. To leading powers in logarithms, this loss is given by their Eq. 31:

$$\Delta \left| \frac{dE}{dx} \right| = \frac{K}{4\pi} \frac{Z}{A} \alpha \left[\ln \frac{2E}{M_\mu c^2} - \frac{1}{3} \ln \frac{2Q_{\max}}{m_e c^2} \right] \ln^2 \frac{2Q_{\max}}{m_e c^2} \quad (4.7)$$

As Kelner *et al.* observe, this addition is important at high energies, amounting to 2% of the ionization loss at 100 GeV and 4% at 1 TeV. It is included in our calculations.

An additional spin-correction term, $(1/4)(Q_{\max}/E)^2$, is included in the square brackets of Eq. (4.2) if the incident particle is a muon (point-like and spin 1/2) [12]. Its contribution to the stopping power asymptotically approaches $0.038 (Z/A) \text{ MeV g}^{-1}\text{cm}^2$, reaching 90% of that value at 200 GeV in most materials. In iron its fractional contribution reaches a maximum of 0.75% at 670 GeV. Although this contribution is well within uncertainties in the total stopping power, its inclusion avoids a systematic bias.

At energies above a few hundred GeV, the maximum 4-momentum transfer to the electron can exceed $1 \text{ GeV}/c$, so that, in the case of incident pions, protons, and other hadrons, cross sections are modified by the extended charge distributions of the projectiles. One might expect this “soft” cutoff to Q_{\max} to reduce the ionization stopping power. This problem has been investigated by J. D. Jackson [11], who concluded that corrections to dE/dx become important only at energies where radiative losses dominate. At lower energies the stopping power is almost unchanged, since its average, dominated by losses due to many soft collisions, is insensitive to the rare hard collisions. For muons the spin correction replaces this form-factor correction.

Jackson and McCarthy [28] have pointed out that the Barkas correction calculated by Fermi (but see their Ref. 20) persists at high energies; to the close-collision part of Eq. (4.9) should be added

$$K z^3 \frac{Z}{A} \frac{\pi \alpha}{2\beta}, \quad (4.8)$$

which is $\pm 0.00176 \text{ MeV g}^{-1} \text{ cm}^2$ for $z = \pm 1$, $Z/A = 1/2$ and $\beta = 1$. This correction produces range differences of a few parts per thousand between positive and negative muons near minimum ionization. At higher energies sign-indifferent radiative effects dominate. We neglect this correction.

4.6. Bethe-Bloch equation

We summarize this discussion with the Bethe-Bloch equation for muons in the form used in this paper:

$$\left\langle -\frac{dE}{dx} \right\rangle = K \frac{Z}{A} \frac{1}{\beta^2} \left[\frac{1}{2} \ln \frac{2m_e c^2 \beta^2 \gamma^2 Q_{\max}}{I^2} - \beta^2 - \frac{\delta}{2} + \frac{1}{8} \frac{Q_{\max}^2}{(\gamma M c^2)^2} \right] + \Delta \left| \frac{dE}{dx} \right| \quad (4.9)$$

The final term, for bremsstrahlung from atomic electrons, is given by Eq. (4.7).

Table 4.1: Comparison of stopping power calculations for protons (in MeV $\text{g}^{-1} \text{cm}^2$) with those of ICRU 49.

	10 MeV	100 MeV	1 GeV	10 GeV
Hydrogen gas ($Z = 1$)				
This calculation	101.7	15.29	4.496	4.539
ICRU 49	101.9	15.30	4.497	4.539
Graphite ($Z = 6$, $\rho = 1.7 \text{ g/cm}^3$)				
This calculation	40.72	6.514	1.942	1.883
ICRU 49	40.84	6.520	1.946	1.881
Iron ($Z = 26$)				
This calculation	28.54	5.045	1.575	1.603
ICRU 49	28.56	5.043	1.574	1.601
Tin ($Z = 50$)				
This calculation	22.26	4.177	1.351	1.426
ICRU 49	22.02	4.165	1.349	1.423
Lead ($Z = 82$)				
This calculation	17.52	3.532	1.189	1.291
ICRU 49	17.79	3.552	1.186	1.288
Uranium ($Z = 92$)				
This calculation	16.68	3.388	1.144	1.243
ICRU 49	16.90	3.411	1.140	1.242
Liquid water				
This calculation	45.94	7.290	2.210	2.132
ICRU 49	45.67	7.289	2.211	2.126

4.7. Comparison with other ionizing energy loss calculations

Comparisons with the ICRU 49 proton tables have been made by running our code with the proton mass. A summary of the stopping power comparisons is given in Table 4.1, and of the CSDA range comparisons in Table 4.2. In general the agreement is regarded as adequate, but is worse at high atomic number and low energy. The simple screening correction given by Eq. (4.4) has been used, and under these conditions somewhat overcorrects.

ICRU 49 compares their tabulated stopping powers for protons at 6.5 and 73 MeV, with the conclusion that differences are “mostly smaller than 1% and hardly ever greater than 2,” and in the case of compounds and mixtures “the uncertainties are approximately three times as large as in the case of elements” [4].

Our muon tables start at $T = 10 \text{ MeV}$, corresponding to a proton energy of about 100 MeV, so that only 100 MeV and above is relevant in the proton comparisons. For uranium the stopping power at 100 MeV is low by 0.8% and the range high by 1.9%. Without the screening correction the stopping power for this case is high by 1.7% and the range low by 2.5%. We make the screening correction only for elements. We conclude that in a worst-case scenario, *e.g.*, PuCl_4 (which we do not tabulate) at 10 MeV, our results could be in error by nearly 3%. For lower- Z materials the agreement is consistent with ICRU 49. In any case the agreement improves rapidly with increasing energy.

Table 4.2: Comparison of CSDA range calculations for protons (in g cm^{-2}) with those of ICRU 49.

	10 MeV	100 MeV	1 GeV	10 GeV
Hydrogen gas				
This calculation	0.0534	3.636	158.7	2254.
ICRU 49	0.0535	3.633	158.7	2254.
Graphite ($Z = 6$, $\rho = 1.7 \text{ g/cm}^3$)				
This calculation	0.1361	8.634	367.4	5333.
ICRU 49	0.1377	8.627	367.0	5337.
Iron ($Z = 26$)				
This calculation	0.2013	11.36	459.2	6383.
ICRU 49	0.2064	11.37	459.6	6389.
Tin ($Z = 50$)				
This calculation	0.2623	13.90	540.9	7272.
ICRU 49	0.2764	13.95	541.9	7291.
Lead				
This calculation	0.3315	16.79	620.7	8120.
ICRU 49	0.3528	16.52	621.7	8143.
Uranium				
This calculation	0.3462	17.56	645.2	8432.
ICRU 49	0.3718	17.24	646.8	8456.
Liquid water				
This calculation	0.1201	7.710	325.4	4703.
ICRU 49	0.1230	7.718	325.4	4700.

Lohmann *et al.* [2] list ionization losses separately for hydrogen, iron, and uranium. Since they do not consider the contributions of bremsstrahlung from atomic electrons (Eq. (4.7)), we have made comparisons with this correction “turned off.” Under these conditions, our results disagree by at most 2 in the 4th decimal place, presumably from different rounding of the density-effect parameters.

5. Radiative losses

5.1. Direct e^+e^- pair production

The cross section for direct e^+e^- pair production in a Coulomb field was first calculated by Racah [29]. Atomic screening was later taken into account by Kelner and Kotov [30]. With their approach, the average energy loss is obtained through a three-fold numerical integration. With the simple parameterization of the screening functions proposed by Kokoulin and Petrukhin [31], one obtains a double differential cross section for e^+e^- production. This formula is widely used in muon transport calculations (for example, see Ref. 2). Based on this work, a (rather complicated) analytic form for the energy spectrum of pairs created in screened muon-nucleus collisions was derived by Nikishov [32]. The explicit formula is given in Appendix B. The average energy loss

for pair production is calculated by numerical integration:

$$b_{\text{pair, nucl}} = -\frac{1}{E} \frac{dE}{dx} \Big|_{\text{pair, nucl}} = \frac{N_A}{A} \int_0^1 v \frac{d\sigma}{dv} dv \quad (5.1)$$

The same expression as for the nucleus is usually used to calculate the pair production contribution from atomic electrons, with Z^2 replaced with Z (*e.g.*, Ref. 2). A more precise approach has recently been developed by Kelner [33], who proposed a simple parameterization of the energy loss based on a rigorous QED calculation. This formula for the electronic contribution to pair production energy loss by muons is valid to within 5% of the more laborious numerical result for $E > 5$ GeV, and is used for the present calculations:

$$b_{\text{pair, elec}} = -\frac{1}{E} \frac{dE}{dx} \Big|_{\text{pair, elec}} = \frac{Z}{A} \left(0.073 \ln \left(\frac{2E/M}{1 + g Z^{2/3} E/M} \right) - 0.31 \right) \times 10^{-6} \text{cm}^2/\text{g} \quad (5.2)$$

Here $g = 4.4 \times 10^{-5}$ for hydrogen and $g = 1.95 \times 10^{-5}$ for other materials.

5.2. Bremsstrahlung

The cross section for electron bremsstrahlung was obtained by Bethe and Heitler [34]. In case of muons, it is necessary to take into account nuclear screening, which was first done consistently by Petrukhin and Shestakov [35]. A simple approximation for medium and heavy nuclei ($Z > 10$) was derived. Lohmann, Kopp, and Voss [2] also used this approximation for $Z < 10$, by setting the nuclear screening correction equal to zero for these cases. As a result, their bremsstrahlung contribution for low- Z nuclei is overestimated by about 10%.

The CCFR collaboration [36] revised the Petrukhin and Shestakov [35] results, pointing out that Ref. 35 overestimates the nuclear screening correction by about 10%. Kelner *et al.* [37] later observed that the CCFR conclusion probably resulted from an incorrect treatment of the Bethe formula. Their new calculations were in good agreement with the old ones by Petrukhin and Shestakov for medium and heavy nuclei, but in addition they proposed an approximation for light nuclei. An independent analysis was performed by the Bugaev group (see, *e.g.*, Ref. 38). The Bethe formula is a particular case of their approach. The Petrukhin and Shestakov and the Bugaev group results for bremsstrahlung on screened nuclei agree to within a few percent.

All of the formulae mentioned above were derived in the Born approximation. It was recently shown [38] that the non-Born corrections in the region of low and high momentum transfers have the same order of magnitude but opposite signs. As a result, they nearly compensate each other.

The differential cross section for muon bremsstrahlung on (screened) nuclei given in Ref. 37 is used for the present paper:

$$\frac{d\sigma}{dv} \Big|_{\text{brems, nucl}} = \alpha \left(2Z \frac{m_e}{M} r_e \right)^2 \left(\frac{4}{3} - \frac{4}{3}v + v^2 \right) \frac{\Phi(\delta)}{v} \quad (5.3)$$

Here v is the fraction of energy transferred to the photon, and

$$\Phi(\delta) = \ln \left(\frac{BMZ^{-1/3}/m_e}{1 + \delta \sqrt{e} B Z^{-1/3}/m_e} \right) - \Delta_n(\delta) , \quad (5.4)$$

where $D_n = 1.54A^{0.27}$, $B = 182.7$ ($B = 202.4$ for hydrogen), $e = 2.7181\dots$, $\delta = M^2 v / 2E(1 - v)$, and the nuclear screening correction Δ_n is given by

$$\Delta_n = \ln \left(\frac{D_n}{1 + \delta (D_n \sqrt{e} - 2) / M} \right) . \quad (5.5)$$

To account for bremsstrahlung losses on atomic electrons, Z^2 in Eq. (5.3) is usually replaced with $Z(Z + 1)$ (*e.g.*, see Ref. 2). A more precise approximation, taking into account electronic binding and recoil, is given by [10],

$$\left. \frac{d\sigma}{dv} \right|_{\text{brems, elec}} = \alpha Z \left(2 \frac{m_e}{M} r_e \right)^2 \left(\frac{4}{3} - \frac{4}{3}v + v^2 \right) \frac{\Phi_{in}(\delta)}{v}. \quad (5.6)$$

In this case

$$\Phi_{in}(\delta) = \ln \left(\frac{M/\delta}{M\delta/m_e^2 + \sqrt{e}} \right) - \ln \left(1 + \frac{m_e}{\delta B Z^{-2/3} \sqrt{e}} \right), \quad (5.7)$$

where $B = 1429$ for all elements but hydrogen, where $B = 446$, and $\delta = M^2 v / 2E(1 - v)$, as above.

The average energy loss $\langle -dE/dx \rangle$ due to bremsstrahlung is calculated by integrating the sum of these cross sections, as in Eq. (5.1).

5.3. Photonuclear interactions

Several approaches have been developed to calculate the muon photonuclear cross section. The most widely used is that of Bezrukov and Bugaev [39]:

$$\begin{aligned} \left. \frac{d\sigma}{dv} \right|_{\text{nuc}} = & \frac{\alpha}{2\pi} A \sigma_{\gamma N}(\varepsilon) v \left\{ 0.75 G(x) \left[\kappa \ln \left(1 + \frac{m_1^2}{t} \right) - \frac{\kappa m_1^2}{m_1^2 + t} - \frac{2M^2}{t} \right] \right. \\ & + 0.25 \left[\kappa \ln \left(1 + \frac{m_2^2}{t} \right) - \frac{2M^2}{t} \right] \\ & \left. + \frac{M^2}{2t} \left[0.75 G(x) \frac{m_1^2}{m_1^2 + t} + 0.25 \frac{m_2^2}{t} \ln \left(1 + \frac{t}{m_2^2} \right) \right] \right\} \end{aligned} \quad (5.8)$$

Here ε is the energy loss of the muon and $\sigma_{\gamma N}(\varepsilon)$ is the photoabsorption cross section defined below. Other values are given by

$$v = \frac{\varepsilon}{E}, \quad t = \frac{M^2 v^2}{1 - v}, \quad \kappa = 1 - \frac{2}{v} + \frac{2}{v^2}, \quad \text{and} \quad G(x) = \frac{3}{x^3} \left(\frac{x^2}{2} - 1 + e^{-x} (1 + x) \right), \quad (5.9)$$

$x = 0.00282 A^{1/3} \sigma_{\gamma N}(\varepsilon)$, $m_1^2 = 0.54 \text{ GeV}^2$, and $m_2^2 = 1.8 \text{ GeV}^2$. This cross section gives results consistent with other calculations to within 30% [2]. Recent measurements of photonuclear interaction of muon in rock performed by the MACRO collaboration [40] agree quite well with Monte Carlo simulations based on the Bezrukov and Bugaev cross section.

The total cross section $\sigma_{\gamma N}(\varepsilon)$ for the photon-nucleon interaction appears as a normalization parameter in Ref. 39, which proposes a simple parameterization:

$$\sigma_{\gamma N}(\varepsilon) \text{ (in } \mu\text{b)} = 114.3 + 1.647 \ln^2(0.0213 \varepsilon) \quad (5.10)$$

This approximation is good enough only for energies $\varepsilon > 5 \text{ GeV}$. For smaller ε , we use the experimental data given by Armstrong *et al.* [41,42]. The energy loss contribution is calculated by numerical integration of the differential cross section given by Eq. (5.8). The use of a more precise photo-absorption cross section for $\varepsilon < 5$ than was used in the original model [39] does not change the photonuclear part of $\langle -dE/dx \rangle$ appreciably.

Table 5.1: Comparison of b_{tot} calculations with those reduced from Lohmann *et al.* [2] and, in the case of standard rock, with Gaisser and Stanev [43]. $10^6 b_{\text{tot}}$ is listed, in units of $\text{g}^{-1} \text{cm}^2$.

Total energy =	10 GeV	100 GeV	1 TeV	10 TeV	100 TeV
Hydrogen gas					
This calculation	0.941	1.345	1.773	2.079	2.284
Lohmann <i>et al.</i>	1.081	1.463	1.814	2.046	—
Carbon					
This calculation	1.278	1.972	2.548	2.859	3.030
*Lohmann <i>et al.</i>	1.3	2.14	2.679	2.958	—
Iron					
This calculation	3.290	5.701	7.392	8.110	8.371
Lohmann <i>et al.</i>	3.312	5.795	7.444	8.128	—
Uranium					
This calculation	8.234	14.614	18.747	20.308	20.760
Lohmann <i>et al.</i>	8.046	14.790	18.870	20.360	—
Water					
This calculation	1.439	2.279	2.959	3.313	3.497
*Lohmann <i>et al.</i>	1.5	2.49	3.125	3.459	—
Standard rock					
This calculation	1.777	2.912	3.779	4.194	4.386
*Lohmann <i>et al.</i>	1.8	3.10	3.960	4.361	—
Gaisser & Stanev	1.91	3.12	4.01	4.40	—
Carlson	2.11	3.19	3.96	4.30	4.38
Oxygen					
This calculation	1.502	2.397	3.108	3.468	3.650
*Lohmann <i>et al.</i>	1.6	2.62	3.290	3.620	—

* Obtained from the Lohmann *et al.* energy loss tables assuming our values for ionization losses (without the bremsstrahlung correction given by Eq. (4.7)). The subtraction loses significance at 10 GeV, where the radiative contribution is small.

5.4. Comparison with other work on muon radiative losses

Selected b values from our present calculations and according to Lohmann *et al.* [2] are plotted in Fig. 5.1 and listed in Table 5.1. Since Lohmann *et al.* did not give the decomposition of the stopping powers except for H, Fe, and U, values of b_{tot} for the materials given in the right half of the figure were obtained by assuming our values of the ionizing losses (without the bremsstrahlung correction given by Eq. (4.7)), which for the fiducial cases agree with their values to within rounding errors in the 4th place.

For $Z > 10$ the results are nearly identical. For smaller atomic number, and at low energies, two effects are responsible for the differences:

1. In the nuclear part of bremsstrahlung, nuclear screening has only a weak energy dependence, and produces about a 4% reduction for hydrogen and a 10% reduction for carbon. This is apparent in our lower values of b_{tot} for carbon and water as compared with Lohmann *et al.*

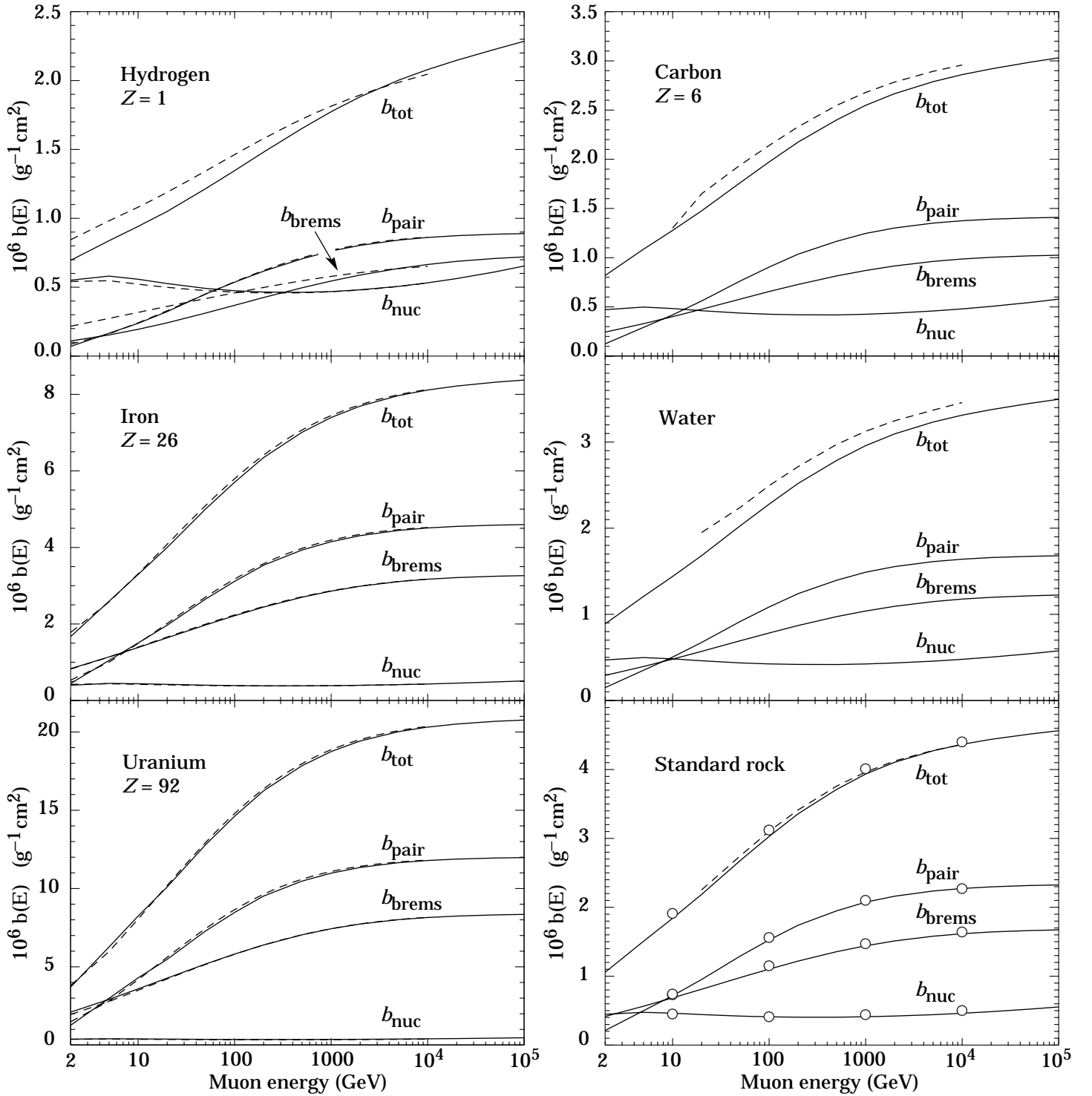


Figure 5.1: b -values for a sampling of materials. The dashed lines are from Lohmann *et al.* [2]. The circles for standard rock are from Gaisser and Stanev [43].

2. Bremsstrahlung from atomic electrons decreases at low energy because of electron recoil. Lohmann *et al.*'s $Z(Z + 1)$ factor is replaced by $Z(Z + 0)$ in the low-energy limit, so that for hydrogen our bremsstrahlung contribution for 1–10 GeV is smaller by nearly a factor of two. Similarly, in the low-energy limit our bremsstrahlung contribution for carbon is 6/7 that of Lohmann *et al.*

The CERN RD 34 collaboration has measured the energy loss spectrum of 150 GeV muons in iron [44]. The energy deposition was measured in prototype hadron calorimeter modules for the ATLAS detector. Most probable ionization loss was subtracted, as was background from photonuclear interactions (which in any case is only about 7% of the total cross section). The remaining sensitivity was to energy loss by pair production (dominant at the smallest energy transfers, $0.01 < v < 0.03$), knock-on electrons (δ rays, included in the high-energy tail of the ionization loss and dominating for $0.03 < v < 0.12$), and bremsstrahlung (dominant for $v > 0.12$). The results, expressed as a fraction of the Kelner *et al.* [10] cross section (basically Petrukhin and Shestakov), are shown in Fig. 5.2. Also shown are the CCFR collaboration's revision of the Petrukhin and Shestakov cross section [36] and Rozental's formula [45], both scaled to the Petrukhin and Shestakov model used in the present calculations. This model describes the data reasonably well, while the others are evidently less successful.

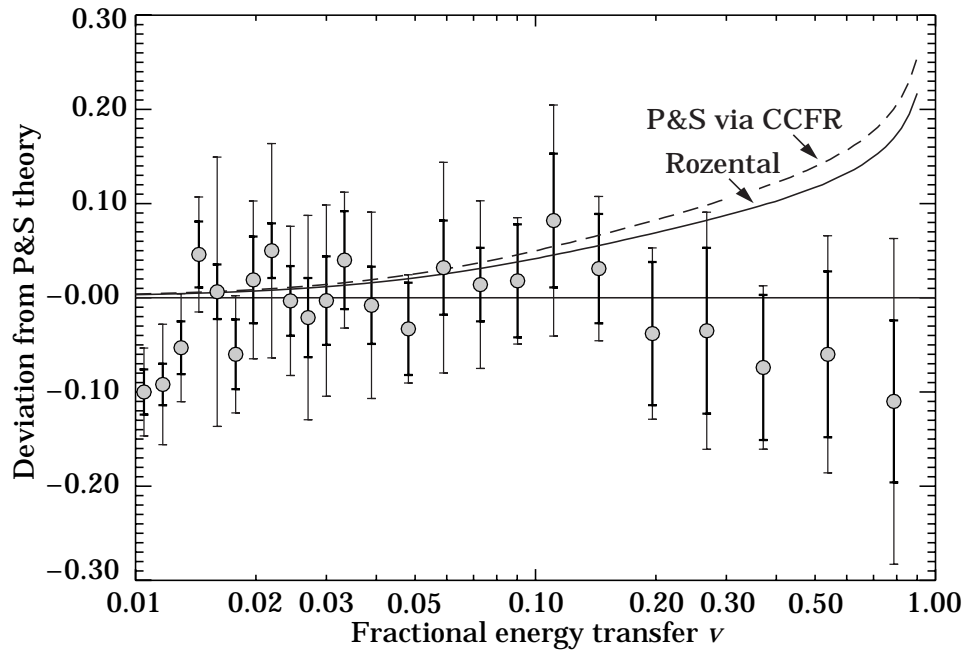


Figure 5.2: RD 34 measurements of radiative losses by 150 GeV muons [44] scaled by the present model, including bremsstrahlung via Kelner *et al.* [10]. Heavy error bars indicate statistical errors only, while the light bars include systematic errors combined in quadrature. Ratios of alternate models including bremsstrahlung using Rozental's formula [45] and the CCFR collaboration's revision of the Petrukhin and Shestakov cross section [36] to our calculations are shown by the solid and dashed lines, respectively.

5.5. Muon critical energy

Equation 1.4 defines the muon critical energy $E_{\mu c}$ as the energy for which ionization and radiative losses are equal. $E_{\mu c}$ for the chemical elements is shown in Fig. 5.3. The equality of ionization and radiative losses comes at a higher energy for gases than for solids and liquids because of the smaller density-effect correction for gases. Fits for gases (excluding hydrogen) and for solids (excluding hydrogen and helium) are shown. Since $E_{\mu c}$ depends upon ionization potentials and density-effect parameters as well as Z , the fits cannot be exact. Alkali metals fall 2.6–3.6% above the fitted function, while most other solids and liquids fall within 2.5% of the fitted function. Among the gases the worst fit is for neon (1.4% high).

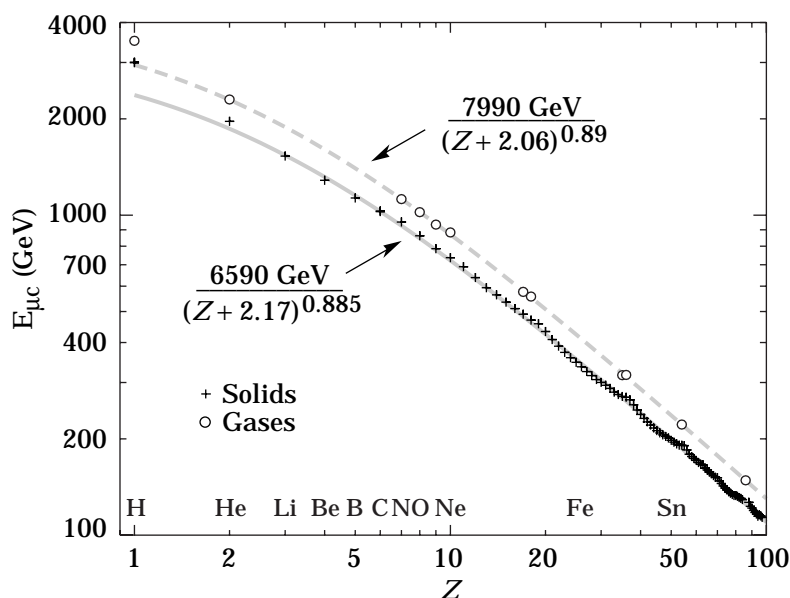


Figure 5.3: Muon critical energy for the chemical elements. As discussed in the text, the fitted functions shown in the figure cannot be exact, and are for guidance only.

Acknowledgments

We wish to thank Felix Boehm (Caltech) for the invitation to write this report. Alberto Fassó (SLAC) was kind enough to make available his ascii files of the density-effect coefficients and composition, which vastly aided verification. Steve Seltzer (NIST) answered our questions and made available code which produced computer-readable files of the main tables of ICRU 49, very much reducing the labor of obtaining these tables. This work was supported by the U.S. Department of Energy under contract No. DE-AC03-76SF00098.

Appendix A. Stopping power and density-effect parameters for compounds and mixtures

For most of the materials for which tables are given in this report, the relevant effective excitation energy and density-effect parameters have already been tabulated, and should be used. This section concerns how to deal with an untabulated compound or mixture.

It is usual to think of a compound or mixture as made up of thin layers of the pure elements (or, better, constituent compounds for which tabulated data are available) in the right proportion (Bragg additivity [46]). Let n_j be the number of the j th kind of atom in a compound (it need not be an integer for a mixture), and w_j its weight fraction:

$$w_j = n_j A_j / \sum_k n_k A_k \quad (\text{Appendix A.1})$$

Then

$$\left\langle \frac{dE}{dx} \right\rangle = \sum_j w_j \left. \frac{dE}{dx} \right|_j \quad (\text{Appendix A.2})$$

When the Bethe-Bloch equation is inserted and the radiative terms added, the Z -dependent terms can be sorted out to find that the mixture or compound is equivalent to a single material with

$$\begin{aligned} \left\langle \frac{Z}{A} \right\rangle &= \sum_j w_j \frac{Z_j}{A_j} = \sum_j n_j Z_j / \sum_j n_j A_j \\ \ln \langle I \rangle &= \sum_j w_j (Z_j/A_j) \ln I_j / \sum_j w_j (Z_j/A_j) = \sum_j n_j Z_j \ln I_j / \sum_j n_j Z_j \\ \langle b(E) \rangle &= \sum_j w_j b_j(E) \end{aligned} \quad (\text{Appendix A.3})$$

There are pitfalls in actually using (Appendix A.3) to calculate $\langle I \rangle$. Since the electrons in a compound are more tightly bound than in the constituent elements, the effective I_j are in general higher than those of the constituent elements. Exceptions are provided by diatomic gases and by metals in metallic alloys or compounds. Berger and Seltzer discuss ways to extend the Bragg additivity rule in lieu of a detailed calculation [17]:

- (a) For a select list of materials (carbon and some common gases), they propose alternate mean excitation energies in their Table 5.1 (or Table 6 in Ref. 17).
- (b) For other elements, the excitation energies are multiplied by 1.13 before calculation of the mean (the “13% rule”). Although it is not said, it would seem sensible to apply this rule in the case of a tightly-bound material such as CsI, and not apply it in the case of a metallic compound like Nb₃Sn.
- (c) Both are superseded by experimental numbers when available, as in the case of SiO₂.

Bragg additivity could be used to calculate the density-effect correction as well, but it would have little meaning. If the material of interest is not available in the Ref. 22 tables, then the algorithm given by Sternheimer and Peierls [23] should be used. Their recipe is given more succinctly in the EGS4 manual [19], and the following algorithm is modified from that version:

- (a) I is obtained as described above
- (b) k is always taken as 3.00
- (c) $\overline{C} = 2 \ln(I/\hbar\omega_p) + 1$, with the plasma energy $\hbar\omega_p$ obtained using the expression from Table 2.1.

(d) For solids and liquids,

$$x_1 = \begin{cases} 2.0 & \text{if } I < 100 \text{ eV, and } x_0 = \begin{cases} 0.2 & \text{if } \overline{C} < 3.681 \\ 0.326 \overline{C} - 1.0 & \text{otherwise} \end{cases} \\ 3.0 & \text{if } I \geq 100 \text{ eV, and } x_0 = \begin{cases} 0.2 & \text{if } \overline{C} < 5.215 \\ 0.326 \overline{C} - 1.5 & \text{otherwise} \end{cases} \end{cases} \quad (\text{Appendix A.4})$$

(e) In the case of gases,

$$x_0 = \begin{cases} 1.6 \text{ and } x_1 = 4.0 & \text{if } \overline{C} < 10.0 \\ 1.7 \text{ and } x_1 = 4.0 & \text{if } 10.0 \leq \overline{C} < 10.5 \\ 1.8 \text{ and } x_1 = 4.0 & \text{if } 10.5 \leq \overline{C} < 11.0 \\ 1.9 \text{ and } x_1 = 4.0 & \text{if } 11.0 \leq \overline{C} < 11.5 \\ 2.0 \text{ and } x_1 = 4.0 & \text{if } 11.5 \leq \overline{C} < 12.25 \\ 2.0 \text{ and } x_1 = 5.0 & \text{if } 12.25 \leq \overline{C} < 13.804 \\ 0.326 \overline{C} - 1.5 & \\ \text{and } x_1 = 5.0 & \text{if } \overline{C} \geq 13.804 \end{cases} \quad (\text{Appendix A.5})$$

(f)

$$a = \frac{\overline{C} - 2 (\ln 10) x_0}{(x_1 - x_0)^3} . \quad (\text{Appendix A.6})$$

We have used this algorithm to calculate the density-effect coefficients for cryogenic liquids, which are not tabulated by Sternheimer, Berger, and Seltzer [22]. In this case, I for the gas was used.

One problem remains: Given the density-effect parameters, either from the literature [22] or from the algorithm given above, how does one modify them for the same material at a different density? This problem occurs for gases at different pressures, or for solid and liquids at different densities than those tabulated. In an early paper [23], Sternheimer noted that under quite general conditions

$$\delta_r(p) = \delta(p\sqrt{r}) , \quad (\text{Appendix A.7})$$

where $r = \rho/\rho_0$, the ratio of desired to tabulated densities, and the subscript r indicates the quantity evaluated at the desired density. This implies [23] that

$$\begin{aligned} \overline{C}_r &= \overline{C} - \ln r \\ x_{0r} &= x_0 - \frac{1}{2} \log_{10} r \\ x_{1r} &= x_1 - \frac{1}{2} \log_{10} r . \end{aligned} \quad (\text{Appendix A.8})$$

It is easily shown by matching different regions in Eq. (4.6) that the parameters a and k are unchanged by the transformation.

This method was used to correct the parameters for several materials to more modern density. For example, in the case of SiO_2 , the tabulated density is incorrect for both crystalline quartz and fused silica.

Both algorithms were checked by calculating $\langle -dE/dx \rangle$ several ways, taking advantage of the fact that Ref. 22 lists both gaseous and liquid helium, three densities of carbon, and both steam and liquid water. The comparisons are discussed at the end of Sect. 4.4.

Appendix B. Direct pair production from screened nuclei

Nikishov's analytic form for the cross section is given by [32]

$$\left. \frac{d\sigma}{dv} \right|_{\text{pair, nucl}} = \frac{(2\alpha r_e Z)^2 (1-v)}{\pi v} \left[(f_1 + \theta f_3) \ln \left(\frac{2k_0}{m_e} \right) + \phi_2 + \theta \phi_4 + I \right], \quad A.1$$

where v is the fraction of energy transferred to the e^+e^- pair and $\theta = m_e^2/M^2$. The functions in the square brackets are given by

$$f_1 + \theta f_3 = \frac{44}{45z} - \frac{16}{45} - \frac{4}{9}\theta - \left(\frac{7}{9} + \frac{8}{45}z + \frac{7}{18}z\theta \right) \ln z \\ + \left[\frac{16}{45}z + \frac{38}{45} - \frac{44}{45z} + \frac{4}{3(z+4)} + \left(\frac{7}{9}z - \frac{2}{9} + \frac{8}{3(z+4)} \right) \theta \right] B(z) \ln \frac{z_2}{z_1}, \quad A.2$$

$$\phi_2 + \theta \phi_4 = \left(\frac{7}{36} + \frac{2}{45}z + \frac{7}{72}z\theta \right) \left(\ln^2 \frac{z_2}{z_1} + \pi^2 + 2 \ln^2 z \right) \\ + \left(\frac{7}{18} + \frac{3}{20}z + \frac{7}{36}z\theta \right) \ln z + \frac{653}{270} - \frac{28}{9z} + \frac{2}{3}\theta \\ + \left[-\frac{3}{10}z - \frac{92}{45} + \frac{52}{45z} - \left(\frac{2}{9} - \frac{7}{18}z \right) \theta \right] B(z) \ln \frac{z_2}{z_1} \\ + B(z) \left[-\frac{8}{45}z - \frac{19}{45} - \frac{8}{45z} - \left(\frac{2}{9} + \frac{7}{18}z \right) \theta \right] \left[\text{Li}_2(y) + 2 \text{Li}_2 \left(\frac{1}{z_2} \right) + \frac{3}{2} \ln^2 \frac{z_2}{z_1} \right] \\ + \left(\frac{8}{z} + z\theta \right) \frac{B(z)}{3(z+4)} \times \left[6 \text{Li}_2 \left(\frac{1}{z_2} \right) - \text{Li}_2(y) + \frac{1}{2} \ln^2 \frac{z_2}{z_1} \right], \quad A.3$$

where

$$z = \frac{v^2}{\theta(1-v)}, \quad z_{1,2} = B(z) \mp \frac{1}{2}, \quad B(z) = \sqrt{\frac{1}{4} + \frac{1}{z}}, \quad y = \frac{z_1 + z_2}{z_2^2},$$

Li_2 is the dilogarithm function (Spence's integral evaluated for $n=2$) [47], and

$$I = \left(\frac{7}{9} + \frac{8}{45}z + \frac{7}{18}z\theta \right) H - \left[\frac{16}{45}z + \frac{38}{45} + \frac{16}{45z} + \left(\frac{7}{9}z + \frac{4}{9} \right) \theta \right] B(z) J_+ \\ + \left[-\frac{16}{45}z - \frac{14}{9} - \frac{8}{9w} + \frac{2}{45} \frac{z}{w} - \frac{4}{5} \frac{z}{w^2} + \frac{2z}{3(w+4)} - \left(\frac{7}{9}z + \frac{4}{9} \frac{z}{w} \right) \theta \right] B(w) I_+ \\ + \left[\frac{32}{45} \frac{u}{w} - \frac{88}{45z} - \frac{16}{45w} + \frac{8}{5} \frac{z}{w^2} + \frac{8}{9} \frac{u}{w} \theta \right] B(u) \ln \frac{u_2}{u_1} \\ + \left[\frac{68}{45} - \frac{16}{45z} + \frac{8}{3w} - \frac{2}{3} \frac{z}{w} - \frac{8}{9} \theta \right] B(z) \ln \frac{z_2}{z_1} + \frac{104}{45z} \\ - \frac{8}{15w} - \frac{62}{27} - \left(\frac{8}{9w} + \frac{1}{45} \frac{z}{w} + \frac{4}{5} \frac{z}{w^2} + \frac{4}{9} \frac{z}{w} \theta \right) \ln z \\ + \left(1 + \frac{1}{2}z\theta \right) \frac{1}{3w} \left(\ln^2 \frac{u_2}{u_1} - \ln^2 \frac{z_2}{z_1} \right) \\ + \left(\frac{8}{z} + z\theta \right) \frac{B(z)}{3(z+4)} - \left[2J_+^{(2)} + \ln^2 z_2 - \ln^2 z_1 \right], \quad A.4$$

where

$$w = s\sqrt{z}, \quad s = \frac{2\sqrt{\gamma\gamma'}Z^{1/3}}{183\sqrt{e}} \approx \frac{\sqrt{\gamma\gamma'}Z^{1/3}}{151}, \\ u = w + z, \quad \gamma = P_0/M, \quad \gamma' = P'_0/M$$

($u_{1,2}$, $B(u)$ and $w_{1,2}$, $B(w)$ are the analogs of $z_{1,2}$, $B(z)$, *i.e.*, $u_{1,2} = B(u) \mp \frac{1}{2}$, *etc.*),

$$\begin{aligned}
H = & \operatorname{Li}_2\left(\frac{z}{u+4}\right) - \operatorname{Li}_2\left(\frac{z+4}{u+4}\right) + \operatorname{Li}_2\left(\frac{z}{z+4}\right) - 2 \operatorname{Li}_2\left(\frac{u}{u+4}\right) \\
& + \operatorname{Li}_2\left(\frac{4w}{u(z+4)}\right) + \operatorname{Li}_2\left(\frac{4z}{u(w+4)}\right) - \operatorname{Li}_2\left(\frac{4}{w+4}\right) + \frac{\pi^2}{6} \\
& + 2 \ln(z_1) \ln(z_2) - 4 \ln(u_1) \ln(u_2) - \ln^2 z + \ln^2(z+4) - \ln\left(1 + \frac{4}{w}\right) \ln(u+4) \\
& - \ln(4w) \ln(z+4) + \ln(16) \ln(u+4) - \ln^2(u+4) + 2 \ln^2 u \\
& + \ln(u) \ln\left(\frac{z+4}{4} \frac{w+4}{4w}\right) - \ln(z) \ln\left(\frac{z+4}{4} \frac{u}{w}\right), \quad J_+ = J_+^{(1)} + J_+^{(2)}, \tag{A.5}
\end{aligned}$$

$$J_+^{(1)} = 2 \operatorname{Li}_2\left(\frac{1}{z_2}\right) - \operatorname{Li}_2(y) + \ln(z_1) \ln \frac{z_2}{z_1}, \quad y = \frac{z_1 + z_2}{z_2^2}, \tag{A.6}$$

$$\begin{aligned}
J_+^{(2)} = & \operatorname{Li}_2\left(\frac{u_1}{z_1}\right) - \operatorname{Li}_2\left(\frac{u_2}{z_2}\right) + \operatorname{Li}_2\left(\frac{z_1}{z_1 + u_2}\right) - \operatorname{Li}_2\left(\frac{z_2}{z_2 + u_1}\right) + \ln\left(\frac{u_1}{z_1}\right) \ln\left(1 - \frac{u_1}{z_1}\right) \\
& - \ln\left(\frac{u_2}{z_2}\right) \ln\left(1 - \frac{u_2}{z_2}\right) + \ln\left(\frac{z_2}{z_i}\right) \ln[u(z_1 + u_2)], \tag{A.7}
\end{aligned}$$

and, finally,

$$\begin{aligned}
I_+ = & \operatorname{Li}_2\left(\frac{u_1}{w_1}\right) - \operatorname{Li}_2\left(\frac{u_2}{w_2}\right) - 2 \operatorname{Li}_2\left(\frac{w_1}{w_2}\right) + \operatorname{Li}_2\left(\frac{w_1}{w_1 + u_2}\right) \\
& - \operatorname{Li}_2\left(\frac{w_2}{w_2 + u_1}\right) + \frac{\pi^2}{3} + \ln\left(\frac{w_2}{w_1}\right) \ln\left(\frac{w_1 + u_2}{w_2} \frac{u}{z}\right) \\
& + \ln\left(\frac{u_1}{w_1}\right) \ln\left(1 - \frac{u_1}{w_1}\right) - \ln\left(\frac{u_2}{w_2}\right) \ln\left(1 - \frac{u_2}{w_2}\right). \tag{A.8}
\end{aligned}$$

References

1. P. H. Barrett, L. M. Bollinger, G. Cocconi, Y. Eisenberg, and K. Greisen, *Rev. Mod. Phys.* **24**, 133 (1952).
2. W. Lohmann, R. Kopp, and R. Voss, “Energy Loss of Muons in the Energy Range 1–10000 GeV,” CERN Report 85–03 (1985).
3. P. J. Mohr and B. N. Taylor, “CODATA Recommended Values of the Fundamental Physical Constants: 1998,” *J. Phys. Chem. Ref. Data*, to be published.
4. “Stopping Powers and Ranges for Protons and Alpha Particles,” ICRU Report No. 49 (1993); Tables and graphs of these data are available at <http://physics.nist.gov/PhysRefData/>.
5. W. H. Barkas, W. Birnbaum, and F. M. Smith, *Phys. Rev.* **101**, 778 (1956).
6. J. Lindhard, *Kgl. Danske Videnskab. Selskab, Mat.-Fys. Medd.* **28**, No. 8 (1954);
J. Lindhard, M. Scharff, and H. E. Schiøtt, *Kgl. Danske Videnskab. Selskab, Mat.-Fys. Medd.* **33**, No. 14 (1963).
7. T. Kaneko, *Atomic Data and Nuclear Data Tables* **53**, 271–283 (1993).
8. H. H. Andersen and J. F. Ziegler, *Hydrogen: Stopping Powers and Ranges in All Elements*. Vol. 3 of *The Stopping and Ranges of Ions in Matter* (Pergamon Press 1977).
9. H. A. Bethe, “Quantenmechanic der Ein- und Zwei-Elektronen Probleme,” p. 273, *Handbuch der Physik*, Vol. 24/1 (Springer-Berlin).
10. S. R. Kelner, R. P. Kokoulin and A. A. Petrukhin, *Phys. Atomic Nuclei* **60**, 576–583 (1997) (*Yad. Fiz.* **60**, 657 (1997)).
11. J. D. Jackson, *Phys. Rev.* **D59**, 017301 (1999).
12. B. Rossi, *High Energy Particles*, Prentice-Hall, Inc., Englewood Cliffs, NJ, 1952.
13. U. Fano, *Ann. Rev. Nucl. Sci.* **13**, 1 (1963).
14. J. D. Jackson, *Classical Electrodynamics*, 2nd ed., John Wiley & Sons, New York, 1975.
15. S. P. Ahlen, *Rev. Mod. Phys.* **52**, 121 (1980).
16. W. H. Barkas and M. J. Berger, *Tables of Energy Losses and Ranges of Heavy Charged Particles*, NASA-SP-3013 (1964).
17. S. M. Seltzer and M. J. Berger, *Int. J. Appl. Radiat.* **33**, 1189–1218 (1982).
18. ICRU Report 37, “Stopping Powers for Electrons and Positrons,” International Commission on Radiation Units and Measurements, Washington, DC (1984).
19. W.R. Nelson, H. Hirayama, and D. W. O. Rogers, “The EGS4 Code System,” SLAC-265, Stanford Linear Accelerator Center (Dec. 1985).
20. W. H. Barkas, N. J. Dyer, and H. H. Heckmann, *Phys. Rev. Lett.* **11**, 26 (1963).
21. M. Agnello *et al.*, *Phys. Rev. Lett.* **74**, 371 (1995).
22. R. M. Sternheimer, M. J. Berger, and S. M. Seltzer, *Atomic Data and Nuclear Data Tables* **30**, 261–271 (1984).
23. R. M. Sternheimer and R. F. Peierls, *Phys. Rev.* **B3**, 3681–3692 (1971).
24. R. M. Sternheimer, *Phys. Rev.* **88**, 851 (1952).

25. S. M. Seltzer and M. J. Berger, *Int. J. Appl. Radiat.* **35**, 665–676 (1984). This paper corrects and extends the results of [17].
26. R. M. Sternheimer, S. M. Seltzer, and M. J. Berger, *Phys. Rev.* **B26**, 6067–6076 (1982);
R. M. Sternheimer, S. M. Seltzer, and M. J. Berger, *Phys. Rev.* **B27**, 6971 (1983) (erratum).
27. S. M. Seltzer, private communication (May 1999).
28. J. D. Jackson and R. L. McCarthy, *Phys. Rev.* **B6**, 4131 (1972).
29. G. Racah, *Nuovo Cim.* **16**, 93 (1937).
30. S. R. Kelner and Yu. D. Kotov, *Sov. Jour. Nucl. Phys.* **7**, 237 (1968) (*Yad. Phys.* **7**, 360 (1968)).
31. R. P. Kokoulin and A. A. Petrukhin, *Acta Physica Acad. Sci. Hung.* 29 Suppl. **4**, 277 (1970).
32. A. I. Nikishov, *Sov. J. Nucl. Phys.* **27**, 677–691 (1978) ((*Yad. Phys.* **27**, 1281–1289 (1978))).
33. S. R. Kelner, *Phys. Atomic Nuclei* **61**, 448 (1998) (*Yad. Phys.* **61**, 511 (1998)).
34. H. A. Bethe and W. Heitler, *Proc. Roy. Soc.* **A146**, 83 (1934).
35. A. V. Petrukhin and V. V. Shestakov, *Can. J. Phys.* **46**, S337 (1968).
36. W. K. Sakumoto *et al.*, *Phys. Rev.* **D45**, 3042 (1992).
37. S. R. Kelner, R. P. Kokoulin and A. A. Petrukhin, preprint MSEPI 024-95, Moscow (1995).
38. Y. M. Andreev and E. V. Bugaev, *Phys. Rev.* **D55**, 1233 (1997).
39. L. B. Bezrukov and E. V. Bugaev, *Sov. J. Nucl. Phys.* **33** 635–643 (1981) (*Yad. Phys.* **33**, 1195–1207 (1981)).
40. E. Scapparone *et al.*, *Nucl. Phys. B, Proc. Suppl.* **75A**, 397–400 (1999).
41. T. A. Armstrong *et al.*, *Phys. Rev.* **D5**, 1640 (1972).
42. T. A. Armstrong *et al.*, *Nucl. Phys.* **B41**, 445 (1972).
43. C. Caso *et al.*, “Review of Particle Physics,” *Eur. Phys. J.* **C3**, 1 (1998);
Also see <http://pdg.lbl.gov>.
44. E. Berger *et al.*, *Z. Phys.* **C73**, 455–463 (1997).
45. I. L. Rozental *Sov. Phys. Uspekhi* **11**, 49 (1968) (*Usp. Phys. Nauk.* **94**, 91 (1968)).
46. W. H. Bragg & R. Kleeman, *Philos. Mag.* **10**, 318 (1905).
47. M. Abramowitz and I. A. Stegun, *Handbook of Mathematical Functions*, National Bureau of Standards Applied Mathematics Series, No. 55, (U. S. Gov. Printing Office, 1964). The dilogarithm (Spence’s integral for $n = 2$) is given by Eq. 27.7.1. CERNLIB routine DDIALOG is used to calculate the function.
48. Commission on Atomic Weights and Isotopic Abundances, *Pure and Appl. Chem.* **68**, 2339 (1996);
G. Audi & A. H. Wapstra, *Nucl. Phys.* **A565**, 1 (1993).
49. M. G. K. Menon and P. V. Ramana Murthy, *Progress In Elementary Particle and Cosmic Ray Physics*, Vol. 9, 161–243 (North Holland, Amsterdam, 1967).
50. *The Reactor Handbook*, 2nd ed. (Edited R. C. Weast), Vol. 1 (Interscience, New York, 1960).

8. Explanation of tables³

TABLE I: Muon energy loss rate and CSDA range for selected chemical elements.

The contents of Table I and other information are given in Table 8.1.

The header defines the element and state, and gives the parameters used to calculate the ionization stopping power:

Z : Atomic number.

A : Atomic weight. The number of significant figures shown varies with element, since isotopic composition of samples varies; in general the atomic weight of elements with only one isotope are known to great precision [48].

ρ : Density. Gas density is evaluated at 20° C.

I : Mean excitation energy.

$a-\delta_0$: Sternheimer *et al.* density effect parameters, as introduced in Sect. 4.4 and Eq. (4.6).

The body of the table presents ionizing energy loss (Eq. (4.9)) and the components of radiative loss rate (see Eqns. 1.1 and 1.2), as well as CSDA range obtained by integrating the total (Eq. (1.5)), as a function of the muon's initial kinetic energy T . The spacing of the independent variable is fairly uniform on a logarithmic scale. The corresponding momentum p is also given. The table is interrupted to show the points at which minimum ionization and muon critical energy (Eq. (1.4)) occur.

TABLE II: Muon energy loss rate and CSDA range for selected compounds and mixtures.

The contents of TABLE II and other information are given in Table 8.2. The format is identical with TABLE I, except that $\langle Z/A \rangle$ (Eq. (Appendix A.3)) replaces Z and A .

TABLE III: b values for the elements listed in TABLE I

Interpolation in $\log E$ is used to generate the b values shown in TABLE I and for the ionizing loss calculations.

TABLE IV: b values for the elements listed in TABLE I

TABLE IV has the same format as TABLE III except that $\langle Z/A \rangle$ replaces Z and A .

³ Computer-readable versions of these tables can be found at http://pdg.lbl.gov/computer_read.html

Table 8.1: Index of tables for selected chemical elements. Physical states are indicated by “G” for gas, “D” for diatomic gas, “L” for liquid, and “S” for solid. Gases are evaluated at one atmosphere and 20° C. The corresponding cryogenic liquids are evaluated at their boiling points at one atmosphere, and carbon is evaluated at several typical densities. Atomic weights are given to their experimental significance. Except where noted, densities are as given by Sternheimer, Berger, and Seltzer [22].

Element	Symbol	Z	A	State	ρ [g/cm ³]	$\langle -dE/dx \rangle_{\min}$ [MeV cm ² /g]	$E_{\mu c}$ [GeV]	$\langle -dE/dx \rangle$ & Range	b	Notes
Hydrogen gas	H	1	1.00794	D	8.375×10^{-5}	4.101	3507.	I- 1	III- 1	
Liquid hydrogen	H	1	1.00794	L	7.080×10^{-2}	4.031	2995.	I- 2	III- 1	1
Helium gas	He	2	4.002602	G	1.663×10^{-4}	1.936	2299.	I- 3	III- 1	
Liquid helium	He	2	4.002602	L	0.125	1.935	1964.	I- 4	III- 1	2
Lithium	Li	3	6.941	S	0.534	1.638	1530.	I- 5	III- 1	
Beryllium	Be	4	9.012182	S	1.848	1.594	1285.	I- 6	III- 1	
Boron	B	5	10.811	S	2.370	1.622	1132.	I- 7	III- 1	
Carbon (compact)	C	6	12.0107	S	2.265	1.744	1022.	I- 8	III- 1	
C (amorphous)	C	6	12.0107	S	2.000	1.748	1026.	I- 9	III- 1	
Carbon (graphite)	C	6	12.0107	S	1.700	1.752	1031.	I-10	III- 1	
Nitrogen gas	N	7	14.00674	D	1.165×10^{-3}	1.824	1122.	I-11	III- 2	
Liquid nitrogen	N	7	14.00674	L	0.807	1.812	952.	I-12	III- 2	2
Oxygen gas	O	8	15.9994	D	1.332×10^{-3}	1.800	1022.	I-13	III- 2	
Liquid oxygen	O	8	15.9994	L	1.141	1.787	862.	I-14	III- 2	2
Fluorine gas	F	9	18.9984032	D	1.580×10^{-3}	1.675	934.	I-15	III- 2	
Liquid fluorine	F	9	18.9984032	L	1.507	1.633	786.	I-16	III- 2	2
Neon gas	Ne	10	20.1797	G	8.385×10^{-4}	1.723	883.	I-17	III- 2	
Liquid neon	Ne	10	20.1797	L	1.204	1.694	736.	I-18	III- 2	2
Sodium	Na	11	22.989770	S	0.971	1.638	690.	I-19	III- 2	
Magnesium	Mg	12	24.3050	S	1.740	1.673	638.	I-20	III- 2	
Aluminum	Al	13	26.981538	S	2.699	1.614	593.	I-21	III- 3	
Silicon	Si	14	28.0855	S	2.330	1.663	563.	I-22	III- 3	
Phosphorus	P	15	30.973761	S	2.200	1.612	535.	I-23	III- 3	
Sulfur	S	16	32.066	S	2.000	1.652	511.	I-24	III- 3	
Chlorine gas	Cl	17	35.4527	D	2.995×10^{-3}	1.629	576.	I-25	III- 3	
Liquid chlorine	Cl	17	35.4527	L	1.560	1.608	490.	I-26	III- 3	2
Argon gas	Ar	18	39.948	G	1.662×10^{-3}	1.519	557.	I-27	III- 3	
Liquid argon	Ar	18	39.948	L	1.396	1.507	470.	I-28	III- 3	2
Potassium	K	19	39.0983	S	0.862	1.622	458.	I-29	III- 4	
Calcium	Ca	20	40.078	S	1.550	1.654	433.	I-30	III- 4	
Titanium	Ti	22	47.867	S	4.540	1.476	389.	I-31	III- 4	
Vanadium	V	23	50.9415	S	6.110	1.436	373.	I-32	III- 4	
Chromium	Cr	24	51.9961	S	7.180	1.455	359.	I-33	III- 4	
Manganese	Mn	25	54.938049	S	7.440	1.427	347.	I-34	III- 4	
Iron	Fe	26	55.845	S	7.874	1.450	336.	I-35	III- 5	
Cobalt	Co	27	58.933200	S	8.900	1.419	324.	I-36	III- 5	
Nickel	Ni	28	58.6934	S	8.902	1.467	315.	I-37	III- 5	
Copper	Cu	29	63.546	S	8.960	1.402	306.	I-38	III- 5	
Zinc	Zn	30	65.39	S	7.133	1.410	300.	I-39	III- 5	
Gallium	Ga	31	69.723	S	5.904	1.378	294.	I-40	III- 5	

Table 8.1: continued

Element	Symbol	<i>Z</i>	<i>A</i>	State	ρ [g/cm ³]	$\langle -dE/dx \rangle_{\min}$ [MeV cm ² /g]	$E_{\mu c}$ [GeV]	$\langle -dE/dx \rangle$ & Range	<i>b</i>	Notes
Germanium	Ge	32	72.61	S	5.323	1.370	287.	I-41	III-6	
Bromine gas	Br	35	79.904	D	7.072×10^{-3}	1.387	316.	I-42	III-6	
Liquid bromine	Br	35	79.904	L	3.103	1.384	271.	I-43	III-6	2
Krypton gas	Kr	36	83.80	G	3.478×10^{-3}	1.357	314.	I-44	III-6	
Liquid krypton	K	36	83.80	G	3.478×10^{-3}	1.356	267.	I-45	III-6	2
Rubidium	Rb	37	85.4678	S	1.532	1.356	265.	I-46	III-6	
Strontium	Sr	38	87.62	S	2.540	1.353	255.	I-47	III-6	
Yttrium	Y	39	88.90585	S	4.469	1.359	246.	I-48	III-6	
Zirconium	Zr	40	91.224	S	6.506	1.348	238.	I-49	III-7	
Niobium	Nb	41	92.90638	S	8.570	1.342	232.	I-50	III-7	
Molybdenum	Mo	42	95.94	S	10.220	1.329	226.	I-51	III-7	
Ruthenium	Ru	44	101.07	S	12.410	1.306	216.	I-52	III-7	
Rhodium	Rh	45	102.90550	S	12.410	1.309	212.	I-53	III-7	
Palladium	Pd	46	106.42	S	12.020	1.288	209.	I-54	III-7	
Silver	Ag	47	107.8682	S	10.500	1.298	206.	I-55	III-8	
Cadmium	Ce	48	112.411	S	8.650	1.276	203.	I-56	III-8	
Indium	In	49	114.818	S	7.310	1.277	201.	I-57	III-8	
Tin	Sn	50	118.710	S	7.310	1.263	198.	I-58	III-8	
Antimony	Sb	51	121.760	S	6.691	1.258	195.	I-59	III-8	
Iodine	I	53	126.90447	S	4.930	1.262	191.	I-60	III-8	
Xenon gas	Xe	54	131.29	G	5.485×10^{-3}	1.255	222.	I-61	III-9	
Liquid xenon	Xe	54	131.29	L	2.953	1.255	191.	I-62	III-9	2
Cesium	Cs	55	132.90545	S	1.873	1.253	190.	I-63	III-9	
Barium	Ba	56	137.327	S	3.500	1.230	184.	I-64	III-9	
Lanthanum	La	57	138.9055	S	6.154	1.230	179.	I-65	III-9	
Cerium	Ce	58	140.116	S	6.657	1.233	176.	I-66	III-9	
Gadolinium	Gd	64	157.25	S	7.900	1.187	162.	I-67	III-9	
Holmium	Ho	67	164.93032	S	8.795	1.169	155.	I-68	III-10	
Hafnium	Hf	72	178.49	S	13.310	1.151	145.	I-69	III-10	
Tantalum	Ta	73	180.9479	S	16.654	1.149	142.	I-70	III-10	
Tungsten	W	74	183.84	S	19.300	1.144	140.	I-71	III-10	
Rhenium	Re	75	186.207	S	21.020	1.142	138.	I-72	III-10	
Osmium	Os	76	190.23	S	22.570	1.131	136.	I-73	III-10	
Iridium	Ir	77	192.217	S	22.420	1.133	135.	I-74	III-11	
Platinum	Pt	78	195.078	S	21.450	1.128	134.	I-75	III-11	
Gold	Au	79	196.96655	S	19.320	1.133	133.	I-76	III-11	
Mercury	Hg	80	200.59	L	13.546	1.130	133.	I-77	III-11	
Lead	Pb	82	207.2	S	11.350	1.122	131.	I-78	III-11	
Bismuth	Bi	83	208.98038	S	9.747	1.127	130.	I-79	III-11	
Thorium	Th	90	232.0381	S	11.720	1.098	121.	I-80	III-12	
Uranium	U	92	238.0289	S	18.950	1.081	118.	I-81	III-12	
Plutonium	Pu	94	244.064197	S	19.840	1.070	114.	I-82	III-12	

Notes:

1. Density effect parameters adjusted to this density using Eq. (*Appendix A.8*).
2. Density effect parameters calculated via the Sternheimer-Peierls algorithm discussed in Appendix A.

Table 8.2: Index of tables for selected compounds and mixtures. Physical states are indicated by “G” for gas, “D” for diatomic gas, “L” for liquid, and “S” for solid. Gases are evaluated at one atmosphere and 20° C. Except where noted, densities are those given by Sternheimer, Berger, and Seltzer [22]. Composition not explained may be found in Seltzer and Berger [17] or in the file `properties.dat` at http://pdg.lbl.gov/computer_read.html.

Compound or mixture	$\langle Z/A \rangle$	State	ρ [g/cm ³]	$\langle -dE/dx \rangle_{\min}$ [MeV cm ² /g]	$E_{\mu c}$ [GeV]	$\langle -dE/dx \rangle$ & Range	b	Notes
Standard rock	0.50000	S	2.650	1.687	671.	II– 1	IV– 1	4
Adipose tissue (ICRP)	0.55947	S	0.920	2.028	1145.	II– 2	IV– 1	
Air	0.49919	G	1.205×10^{-3}	1.815	1085.	II– 3	IV– 1	
Aluminum oxide	0.49038	S	3.970	1.646	683.	II– 4	IV– 1	
Barium fluoride (BaF ₂)	0.42207	S	4.890	1.302	221.	II– 5	IV– 1	
Bismuth germanate (Bi ₄ Ge ₃ O ₁₂)	0.42065	S	7.130	1.250	173.	II– 6	IV– 1	
Blood (ICRP)	0.54995	L	1.060	1.970	999.	II– 7	IV– 2	
Compact bone (ICRU)	0.53010	S	1.850	1.848	809.	II– 8	IV– 2	
Cortical bone (ICRP)	0.52130	S	1.850	1.802	725.	II– 9	IV– 2	
Brain (ICRP)	0.55423	S	1.030	1.989	1012.	II–10	IV– 2	
Butane (C ₄ H ₁₀)	0.59497	G	2.493×10^{-3}	2.277	1513.	II–11	IV– 2	
Calcium carbonate (CaCO ₃)	0.49955	S	2.800	1.685	611.	II–12	IV– 2	
Calcium oxide (CaO)	0.49929	S	3.300	1.649	491.	II–13	IV– 3	
Carbon dioxide	0.49989	G	1.842×10^{-3}	1.818	1065.	II–14	IV– 3	
Carbon dioxide, solid (dry ice)	0.49989	S	1.563	1.786	898.	II–15	IV– 3	2
Cesium iodide (CsI)	0.41569	S	4.510	1.242	188.	II–16	IV– 3	
Concrete (shielding)	0.50274	S	2.300	1.710	678.	II–17	IV– 3	5
Diethyl ether (CH ₃ CH ₂) ₂ O)	0.56663	L	0.714	2.070	1181.	II–18	IV– 3	
Ethane (C ₂ H ₆)	0.59861	G	1.253×10^{-3}	2.303	1558.	II–19	IV– 4	
Ethyl alcohol (C ₂ H ₅ OH)	0.56437	L	0.789	2.053	1140.	II–20	IV– 4	
Eye lens (ICRP)	0.54977	S	1.100	1.969	1023.	II–21	IV– 4	
Borosilicate glass (Pyrex Corning 7740)	0.49707	S	2.230	1.695	708.	II–22	IV– 4	
Lead glass	0.42101	S	6.220	1.255	171.	II–23	IV– 4	
Plate glass	0.49731	S	2.400	1.683	650.	II–24	IV– 4	
Lithium fluoroide (LiF)	0.46262	S	2.635	1.613	875.	II–25	IV– 5	
Lithium iodide (LiI)	0.41939	S	3.494	1.272	202.	II–26	IV– 5	
Lung (ICRP)	0.54965	S	1.050	1.969	998.	II–27	IV– 5	
Methane (CH ₄)	0.62334	G	6.672×10^{-4}	2.416	1668.	II–28	IV– 5	
Methanol (CH ₃ OH)	0.56176	L	0.791	2.037	1099.	II–29	IV– 5	
Skeletal muscle (ICRP)	0.54938	S	1.040	1.969	999.	II–30	IV– 5	
Striated muscle (ICRU)	0.55005	S	1.040	1.972	999.	II–31	IV– 6	
Nylon (type 6, 6/6) (NH(CH ₂) ₅ CO) _n)	0.54790	S	1.180	1.972	1119.	II–32	IV– 6	1, 3
Octane (C ₈ H ₁₈)	0.57778	L	0.703	2.122	1269.	II–33	IV– 6	
Paraffin (CH ₃ (CH ₂) _{n≈23} CH ₃)	0.57275	S	0.930	2.086	1245.	II–34	IV– 6	
Polyvinylchloride (PVC) (C ₂ H ₃ Cl) _n	0.51201	S	1.300	1.778	675.	II–35	IV– 6	
Polyvinyl tolulene (scintillator)	0.54141	S	1.032	1.955	1156.	II–36	IV– 6	
Plutonium dioxide (PuO ₂)	0.40583	S	11.460	1.157	134.	II–37	IV– 7	
Polyethylene ((C ₂ H ₄) _n)	0.57034	S	0.890	2.078	1240.	II–38	IV– 7	1, 3
Polyethylene terephthalate (Mylar)	0.52037	S	1.400	1.847	1017.	II–39	IV– 7	
Polymethyl methacrylate (Acrylic)	0.53937	S	1.190	1.928	1071.	II–40	IV– 7	
Polystyrene (C ₆ H ₅ CHCH ₂) _n	0.53768	S	1.150	1.931	1142.	II–41	IV– 7	1
Polytetrafluoroethylene (Teflon) (C ₂ F ₄) _n	0.47992	S	2.200	1.670	827.	II–42	IV– 7	

Table 8.2: continued

Compound or mixture	$\langle Z/A \rangle$	State	ρ [g/cm ³]	$\langle -dE/dx \rangle_{\min}$ [MeV cm ² /g]	$E_{\mu c}$ [GeV]	$\langle -dE/dx \rangle$ & Range	b	Notes
Propane (C ₃ H ₈)	0.58962	G	1.879×10^{-3}	2.261	1514.	II-43	IV- 8	
Liquid propane (C ₃ H ₈)	0.58962	L	0.430	2.196	1321.	II-44	IV- 8	
n-propyl alcohol (C ₃ H ₇ OH)	0.56577	L	0.803	2.061	1162.	II-45	IV- 8	
Silicon dioxide (fused quartz) (SiO ₂)	0.49930	S	2.200	1.698	686.	II-46	IV- 8	1, 3
Silicon dioxide (crystalline quartz)	0.49930	S	2.648	1.692	682.	II-47	IV- 8	1
Skin (ICRP)	0.54932	S	1.100	1.968	1024.	II-48	IV- 8	
Sodium iodide (NaI)	0.42697	S	3.667	1.304	218.	II-49	IV- 9	
Stilbene (C ₆ H ₅)CHCHC ₆ H ₅)	0.53260	S	0.971	1.922	1134.	II-50	IV- 9	
Testes (ICRP)	0.55108	S	1.040	1.975	1000.	II-51	IV- 9	
Soft tissue (ICRP)	0.55121	S	1.000	1.981	1029.	II-52	IV- 9	
Soft tissue (ICRU four-component)	0.54975	S	1.000	1.971	1008.	II-53	IV- 9	
Liquid water (H ₂ O)	0.55509	L	1.000	1.990	998.	II-54	IV- 9	
Water vapor (H ₂ O)	0.55509	G	7.562×10^{-4}	2.051	1197.	II-55	IV-10	

Notes:

1. Density effect parameters adjusted to this density using Eq. (*Appendix A.8*).
2. Density effect parameters calculated via the Sternheimer-Peierls algorithm discussed in Appendix A.
3. Actual density may vary from the nominal value listed.
4. For at least two generations, the depth of underground muon experiments has been reduced to depth in “standard rock.” This is by definition the overburden of the Cayuga Rock Salt Mine near Ithaca, New York, where K. Greisen and collaborators made seminal observations of muons at substantial depths [1]. Ref. 1 says only “Most of the ground consists of shales of various types, with average density 2.65 g/cm² and average atomic number 11.” Menon and Murthy later extended the definition: $\langle Z^2/a \rangle = 5.5$, $\langle Z/A \rangle = 0.5$, and $\rho = 2.65$ g/cm² [49]. It was thus not-quite-sodium. Lohmann *et al.* [2] further assumed the excitation energy and density effect parameters of calcium carbonate, with no adjustments for the slight density difference. We use their definition for this most important material.
5. Concrete is a very ill-defined material. The composition given in Ref. 17 and on the web page is from the *Reactor Handbook* [50].